analytical chemistry

pubs.acs.org/ac Article

On-Demand Submetabolome Profiling of Early Ferroptosis with Porous Polymeric Magnetic Chemoselective Probes

Haijie Wang, Qian An, Wenxin Wang, Hao Zhou, Youping Deng, Yu-Qi Feng, Wei-Hai Chen,* Zhenwei Wei,* and Xiangyu Wang*

Cite This: *Anal. Chem.* 2025, 97, 26830−26841 Read Online

ACCESS | Metrics & More | Article Recommendations | Supporting Information

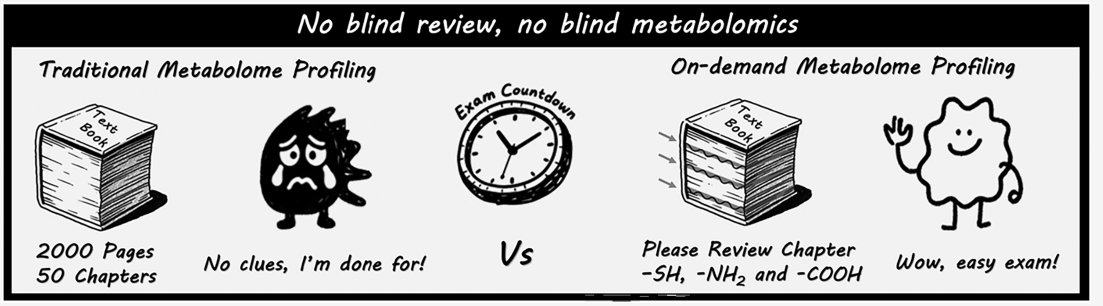

ABSTRACT: Emerging evidence has linked ferroptosis to major chronic diseases such as neurodegenerative and cardio-vascular disorders. Understanding the early stage metabolic network during ferroptosis is essential for uncovering disease mechanisms and developing therapeutic strategies. As oxidative stress occurs in the early phase of ferroptosis, me-tabolites bearing thiol, amino, and unsaturated carboxyl groups may undergo significant changes. However, their comprehensive profiling remains challenging. Here, we developed a boron beacon−based magnetic chemoselective probe for the targeted enrichment, labeling, and simultaneous mass spectrometric analysis of carboxyl-, amino-, and thiol-containing metabolites in complex biological environments. Compared to conventional probes, our design offers significantly faster reaction kinetics, higher labeling efficiency, and a streamlined workflow. Moreover, the boron-based probes generate distinct isotopic patterns in MS^1 and diagnostic fragments in MS^2 spectra, enabling precise submetabolome targeting and characterization. Using this strategy, we performed submetabolome profiling of HeLa cells undergoing ferroptosis and identified 303 dysregulated metabolites. The results revealed coordinated perturbations in key metabolic pathways, including transsulfuration, fatty acid biosynthesis, and glutathione metabolism. This work not only provides mechanistic insights into ferroptosis regulation but also establishes a high-throughput and functionally guided platform for metabolomic network analysis for future studies.

INTRODUCTION

Ferroptosis plays a critical role in the pathogenesis of neurodegenerative and cardiovascular diseases, offering opportunities for precise diagnosis and therapy.[1−4] As an iron-dependent form of regulated cell death,[5,6] ferroptosis is tightly linked to cellular redox homeostasis.[7,8] Disruption of iron metabolism induces severe oxidative stress,[9] leading to rapid reactive oxygen species (ROS) accumulation, glutathione (GSH) depletion, and inactivation of antioxidant defenses such as GPX4—events marking the first phase of ferroptosis.[1,10−12] Continued stress triggers Fenton reactions involving Fe^{2+}, further increasing ROS and causing irreversible lipid peroxidation of polyunsaturated fatty acids (PUFAs), ultimately resulting in cell death.[1,12−15] Before this point of no return, cells may enter a transient, reversible phase involving antioxidant repair.[16] For instance, the transsulfuration pathway supports cysteine supply for redox defense,[17] while metabolites such as serotonin and 3-hydroxyanthranilic acid act as radical-trapping antioxidants that directly quench lipid peroxyl radicals.[18] These findings highlight ferroptosis as a progressive and metabolically coordinated process. Profiling metabolic changes in its early phase is essential for understanding disease mechanisms and identifying targets for early intervention.

Fluorescence and mass spectrometry (MS) are currently the primary methods for ferroptosis analysis. A variety of fluorescent probes have been developed to monitor intracellular iron levels,[19] ROS,[20−22] lipid peroxidation,[23] and GSH.[24,25] However, constrained by the limited number of spectral detection channels, these probe techniques are

Received: September 18, 2025
Revised: November 17, 2025
Accepted: November 18, 2025
Published: November 25, 2025

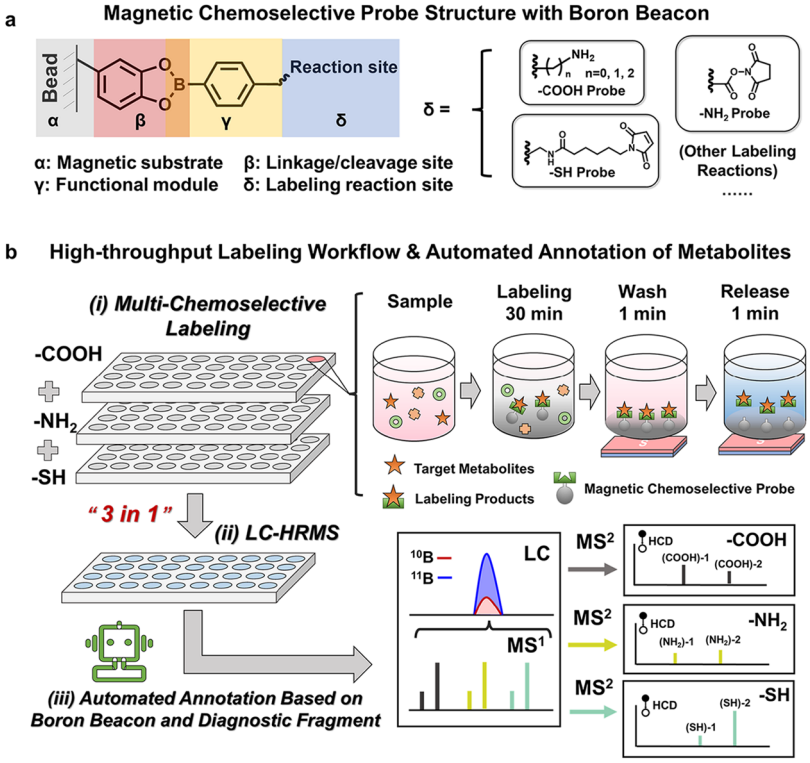

Figure 1. Schematic illustration of the magnetic chemoselective probe structure and labeling strategy workflow. (a) Structure of the magnetic chemoselective probe, composed of a Fe_3O_4 magnetic nanoparticle core with porous polymeric shell, a pH-responsive boronic ester linker, and functional reactive groups for selective labeling of thiol, amino, and carboxyl metabolites, respectively. (b) Workflow of high-throughput submetabolome analysis using magnetic chemoselective probes coupled with LC-HRMS. Three classes of probes targeting carboxyl, amino, and thiol groups are individually incubated with the sample to enable rapid labeling and enrichment. After incubation, magnetic separation allows for efficient washing and release of the labeled metabolites. The boron element embedded in the probes serves as an MS^1-level beacon for product identification, while each functional group-specific tag yields unique MS^2 fragment ions. This enables pooling of the three labeled samples and a single LC-HRMS run to achieve comprehensive submetabolome profiling.

inadequate for mapping complex multitype metabolic networks, but are particularly adept at in situ real-time monitoring of specific metabolites. MS-based ferroptosis studies have mainly focused on untargeted lipidomics to detect lipid peroxidation.[26−28] Yet, these approaches often suffer from limited sensitivity and unsatisfied metabolite coverage,[29,30] with few reports addressing early stage metabolic changes. During the early phase of ferroptosis, cells undergo extensive oxidative stress. Functional groups such as thiols, amines, and unsaturated carboxylic acids—critical for maintaining redox homeostasis—may play key roles in this process. Thus, chemoselective submetabolome profiling targeting these metabolite classes could significantly enhance the depth and coverage of early ferroptosis-related metabolic analysis, providing new insights into its underlying biological mechanisms.

Chemoselective probes have become essential tools in submetabolome studies due to their ability to simultaneously remove matrix interference and selectively label and enrich target metabolites.[31−35] With growing interest in multiclass metabolomics, single-cell metabolomics, and spatial metabolomics,[36−38] there is increasing demand for chemoselective probes with higher throughput, broader metabolite coverage, and simplified workflows in the recent years. Early probes often employed silica beads or nanoparticles as solid substrates. However, the slow kinetics of solid−liquid phase reactions required extended labeling times, limiting analytical throughput.[35,39−41] To address this, we previously developed monolithic polymer probes with hierarchical channels and mesoporous structures, which significantly accelerated labeling kinetics and reduced reaction time from several hours to under 10 min.[42] To further simplify the workflow, Globisch and other workers introduced magnetic nanoparticle-based chemoselective probes, enabling magnetic separation and reducing the need for repeated centrifugation steps.[35,43−45] To address the need for cross-class metabolic profiling,[46,47] we previously demonstrated that a probe design strategy based on boronate cleavage sites could be extended to the detection of multiple categories of metabolites.[42] More recently, Li et al. reported a parallel labeling strategy that enables broad coverage of carboxyl, amino, thiol, and carbonyl groups,[48] while Zhou et al. used hydrazine-based probes to simultaneously label carboxyl, carbonyl, and phosphate-containing metabolites.[49] In another example, Globisch et al. developed a dual-function probe using 4-nitrophenyl-2H-azirine reagents to convert carboxylic acids into carbonyls, allowing simultaneous analysis of carboxyl and carbonyl metabolites with a single probe.[50]

In this study, we aimed to integrate the fast labeling capability of boronic acid-functionalized monolithic polymer-based probes with the streamlined workflow of magnetic probes to address the submetabolome profiling needs of thiol-, amine-, and carboxyl-containing metabolites during early ferroptosis (Figure 1). To this end, we developed a highly integrated chemoselective probe by coating porous organic polymers onto Fe_3O_4 magnetic nanoparticles. The labeling reagent utilizes its boronic acid groups as a modular anchor for

https://doi.org/10.1021/acs.analchem.5c05834
Anal. Chem. 2025, 97, 26830−26841

pH-controlled, cleavable boronate ester binding to a magnetic polymer, ensuring the released product carries a boron-coded MS tag. We introduced maleimide, succinimidyl ester, and amine groups to selectively label thiol (-SH), amine (-NH_2), and carboxyl metabolites (-COOH), respectively. The magnetic core enables rapid and parallelizable separation in multiwall plates, allowing for high-throughput, in situ labeling and matrix removal from cell samples. Thanks to the interconnected porous architecture, confinement effects, and high density of reactive sites, labeling time for all three metabolite classes was reduced from hours to just 30 min. More importantly, the labeled products of thiol, amine, and carboxyl compounds each exhibit distinct features: (1) all carry boron-containing tags with characteristic isotopic signatures, enhancing their MS detectability at the MS^1 level; (2) upon MS^2 fragmentation, each class yields unique diagnostic fragment ions. This enables a "three-in-one" analysis strategy: by pooling all labeled products, a single LC−MS/MS run is sufficient to distinguish metabolite subclasses based on their MS^2 signatures—eliminating the need for separate analyses and significantly boosting analytical throughput.

EXPERIMENTAL SECTION

Chemicals and Materials and Synthesis of Thiol- and Amino-labeling Reagents. All carboxyl-, amino-, and thiol-containing standards were purchased from Titan Technology Co., Ltd. (Shanghai, China), Bidepharm Technology Co., Ltd. (Shanghai, China), Meryer Biochemical Technology Co., Ltd. (Shanghai, China), Bide Pharmatech Co., Ltd. (Shanghai, China), and Aladdin Biochemical Technology Co., Ltd. (Shanghai, China), with detailed information provided in Table S1. Fe_3O_4 nanoparticles (100 nm), tetraethyl orthosilicate (TEOS), 2-chloro-1-methylpyridinium iodide (CMPI), and triethylamine (TEA) were obtained from Meryer Biochemical Technology Co., Ltd. (Shanghai, China). γ-methacryloxypropyltrimethoxysilane (γ-MPS), ethylene dimethacrylate (EGDMA), 2,2′-azobis(2-methylpropionitrile) (AIBN) and N,N-diisopropylethylamine (DIEA) were purchased from Macklin Biochemical Technology Co., Ltd. (Shanghai, China). 3-methacrylamide-dopamine (3-MDA), 6-maleimidohexanoic acid, O-Benzotriazole-N,N,N′,N′-tetramethyl-uronium-hexafluorophosphate (HBTU), 1-hydroxybenzotriazole (HOBT), 4-(aminomethyl) phenylboronic acid hydrochloride, 4-carboxyphenylboronic acid, 3-[(Ethylimino)-methylidene]amino-N,N-dimethylpropan-1-amine (EDCI), *N*-hydroxysuccinimide, and 4-(2-aminoethyl) phenylboronic acid hydrochloride were purchased from Bide Pharmatech Co., Ltd. (Shanghai, China). Additional reagents are detailed in the Supporting Information. Thiol- and amino-labeling reagents were synthesized according to previously established procedures.[42]

Preparation of Magnetic Chemoselective Probes. Synthesis of magnetic substrate Fe_3O_4@SiO_2@P(3-MDA-*co*-EGDMA) modified from reported work.[51] Silica coating was first performed via the Stöber method: 500 mg commercial Fe_3O_4 nanoparticles were ultrasonically dispersed in 25 mL purified water, then added to a mixture of TEOS (20 mL), NH_4OH (25 mL), H_2O (221.67 mL), and EtOH (778.33 mL) in a 2 L three-neck flask. The reaction proceeded at 500 rpm (RT, 12 h). The resulting Fe_3O_4@SiO_2 was alternately washed with methanol/H_2O and dried under N_2 flow. For vinyl group functionalization, 500 mg Fe_3O_4@SiO_2 was dispersed in toluene (205 mL) by sonication, followed by addition of 450 mg γ-MPS. After stirring at 300 rpm (RT, 24 h), the product was washed (methanol/H_2O) and N_2-dried. Distillation−precipitation polymerization was then conducted by dispersing 500 mg vinyl-modified particles in ACN (192 mL) with 3-MDA (504 mg), EGDMA (583 mg), and AIBN (7.5 mg). The mixture was heated from 50 °C to ACN reflux over 30 min, distilling 50% solvent within 2 h. After cooling to RT, Fe_3O_4@SiO_2@P(3-MDA-*co*-EGDMA) was magnetically separated, washed (methanol/H_2O), and N_2-dried.

Probe functionalization was achieved by incubating 20 mg washed magnetic substrate with 1 mL solutions (5 mg/mL in ACN) of carboxyl-, amino-, or thiol-labeling reagents at RT for 3 h. The resulting probes—designated MCP(COOH), MCP-(NH_2), and MCP(SH)—were washed with ACN and dried under N_2 flow.

Cell Ferroptosis Model Establishment. HeLa cells were purchased from Procell Life Science & Technology Co., Ltd. (Wuhan, China) and routinely cultured in MEM complete medium supplemented with 10% fetal bovine serum (FBS) and 1% penicillin-streptomycin at 37 °C under 5% CO_2. When reaching 80% confluency, cells were harvested using trypsin-EDTA and seeded at densities of 1×10^4 cells/well in 96-well plates or 5×10^5 cells/well in 6-well plates. For ferroptosis model optimization, HeLa cells in 96-well plates were treated with 0.5, 1, 3, 5, 7, 10, or 15 μmol/mL Erastin (dissolved in MEM complete medium) for 12 h after 24 h of culture and PBS washing. Cell viability assessed by CCK-8 assay. Time-course samples were prepared by treating HeLa cells in 96-well plates with 7 μmol/mL Erastin for 0−24 h (1, 2, 3, 4, 5, 6, 8, 10, 12, 14, 16, 20, 24 h). Triplicate wells were designated for thiol-, amino-, and carboxyl-group metabolites at each time point, with three independent replicates per group. Details of the cell model validation experiments are described in the Supporting Information.

Metabolite Extraction and Labeling Procedure. Post-treatment HeLa cells (~1×10^5) were trypsinized, centrifuged (10,000 rpm, 10 min, 4 °C), washed with PBS, and extracted with 0.7 mL acetonitrile (ACN) via ice-bath ultrasonication for 30 min. Supernatants were collected after centrifugation.

Two experimental sets (labeled and unlabeled) were processed post-Erastin treatment. For labeled groups: 500 μL sample was treated in parallel—carboxyl group: 60 μL 20 μmol/mL CMPI, 60 μL 20 μmol/mL TEA, 20 mg MCP-(COOH); amino group: 60 μL 20 μmol/mL TEA, 30 mg MCP(NH_2); thiol group: 30 mg MCP(SH). After 30 min incubation at room temperature, probes were magnetically separated, washed with 1 mL ACN, and eluted with acidic eluent (ACN/0.1 M HCl, 9:1 v/v; carboxyl/thiol: twice; amino: four times). Combined eluates were dried under nitrogen and reconstituted in 100 μL ACN/H_2O (3:7 v/v) for LC-HRMS. Unlabeled groups: 500 μL extract was dried and reconstituted in 100 μL ACN/H_2O (3:7 v/v) for direct LC-HRMS.

Analysis Condition. For labeled samples, full-scan analysis was performed in positive mode, with an m/z scan range of 110−1000 Th at the resolution of 120,000. The optimized ESI source parameters were: capillary temperature, 325 °C; spray voltage, 3.5 kV; sheath gas pressure, 50 psi; auxiliary gas pressure, 10 psi; heater temperature, 350 °C; S-Lens RF level, 40%; and intensity threshold, 2×10^4. MS^2 data were acquired in a data-dependent acquisition (DDA) mode using HCD with a collision energy of 30 eV, resolution of 30000, and scan range

https://doi.org/10.1021/acs.analchem.5c05834
Anal. Chem. 2025, 97, 26830−26841

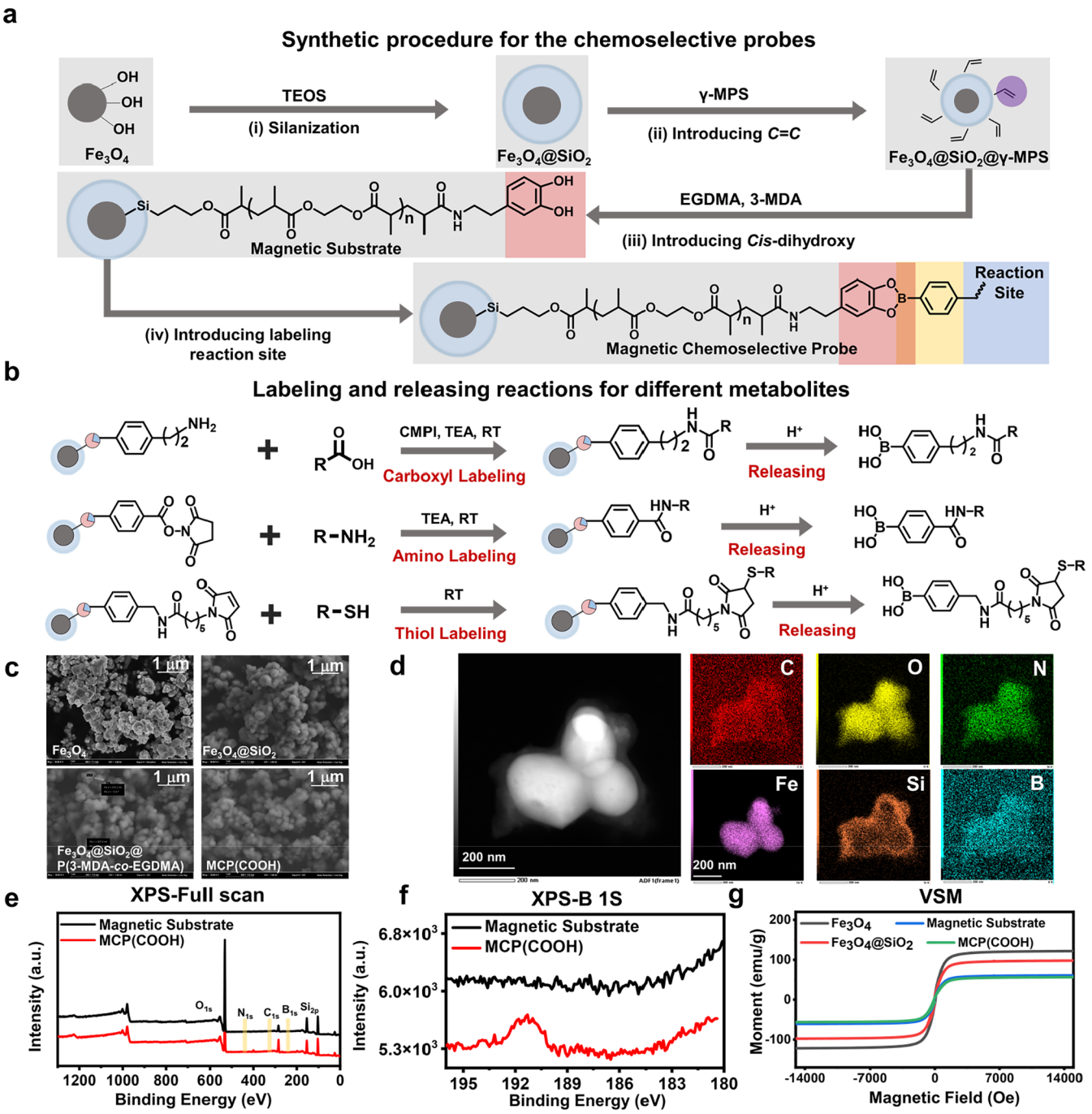

Figure 2. Fabrication and characterization of the magnetic chemoselective probe. (a) Schematic diagram of the preparation process of the magnetic chemoselective probe. (b) Reaction schemes of three probes bearing amino, succinimidyl, and maleimide labeling groups for selective labeling of carboxyl, amino, and thiol metabolites, respectively. Characterization of the probes (figure shows the carboxyl-reactive probe as a representative example). (c) SEM images show a morphological transition during the synthesis process, with particle size increasing from ∼100 to ∼350 nm after stepwise modification. (d) EDS analysis confirms the presence of six elements (C, O, N, Fe, Si, and B) on the probe surface and EDS mapping of Si showed a clear silica shell with a thickness of ∼50 to 100 nm. (e) XPS-Full scan spectra demonstrate higher C 1s and N 1s peak intensities in the probe relative to the magnetic substrate, confirming elevated carbon and nitrogen content on the probe surface. (f) XPS results of B 1s confirms successful introduction of boron-containing moieties on probe surface after modification. (g) VSM hysteresis loops reveal a decrease in saturation magnetization from 121.9 to 56.2 emu/g across steps i−iv.

of 50−1000 Th. Analytical conditions for other experiments are detailed in the Supporting Information.

Methodological Validation. Versatility of probe labeling performance was assessed by labeling structurally diverse carboxyl-, amino-, and thiol-compounds (Table S1) in a 1 μg/mL mixed standard solution through CMPI/TEA-mediated coupling, NHS-activated esterification, and thiol-maleimide click chemistry, respectively. MS^2 fragmentation patterns under high-energy collision dissociation (HCD) were characterized at 20, 30, and 40 eV collision energies. Limits of detection (LODs) and quantification (LOQs), defined as signal-to-noise ratios ≥3 and ≥10, established sensitivity thresholds. Method

https://doi.org/10.1021/acs.analchem.5c05834
Anal. Chem. 2025, 97, 26830−26841

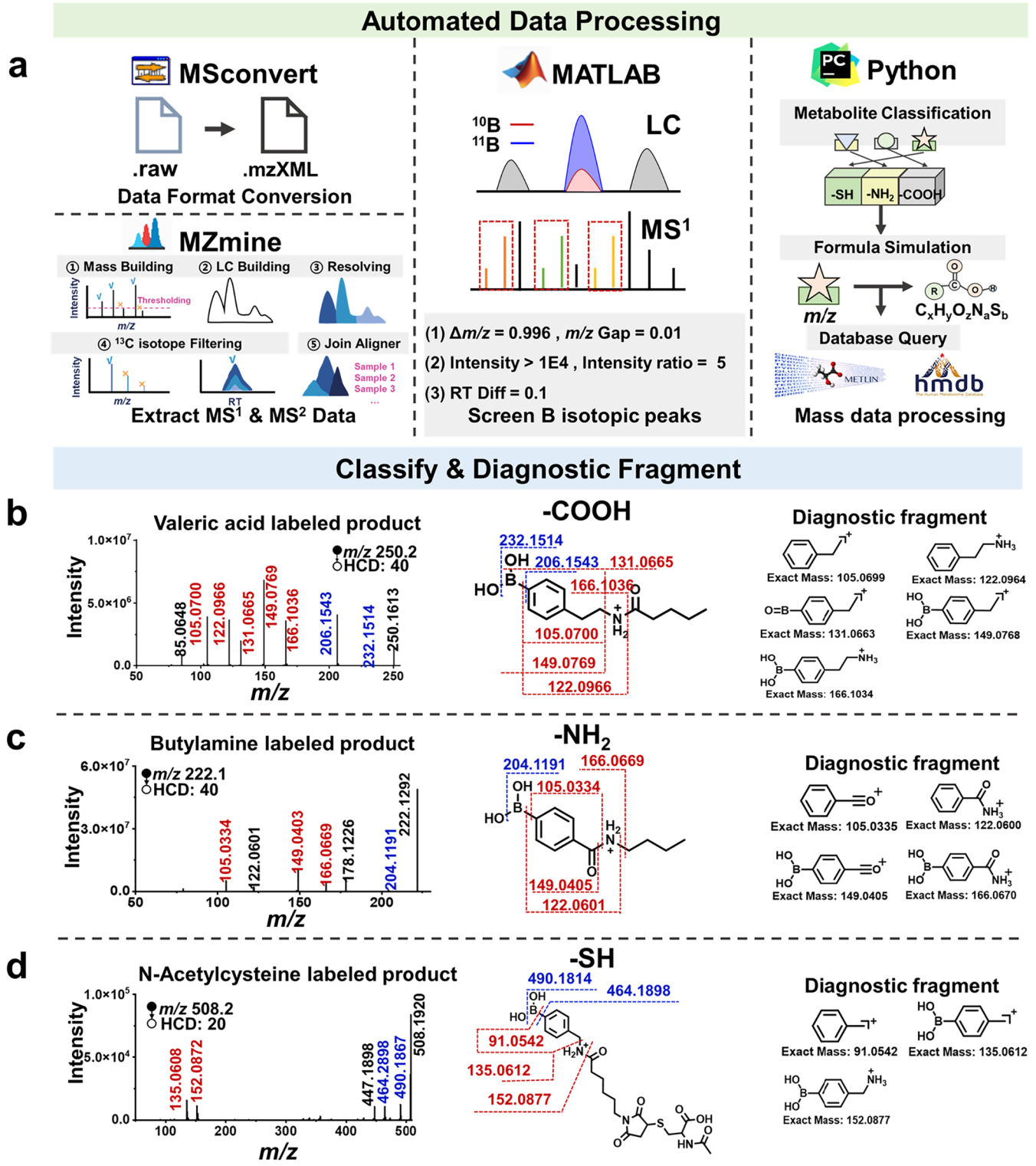

Figure 3. Automated data process and diagnostic MS^2 fragment ions for metabolites classification. (a) Raw data files were converted using MSconvert and processed with MZmine to extract accurate m/z, retention time, and intensity from both MS^1 and MS^2 spectra. MS^2 data were screened using a custom MATLAB script to identify features with boron isotope signatures, while MS^2 data were processed using a Python-based algorithm for metabolite classification. Representative MS^2 fragmentation spectra of labeled valeric acid (b), butylamine (c), and N-acetylcysteine (d), highlighting functional group-specific diagnostic fragment ions for carboxyl, amino, and thiol labeling, respectively.

stability was evaluated using HeLa cell extracts spiked with 2 μg/mL standards—valeric/butyric/mercaptobutyric acids (carboxyls), methionine/cyclohexylamine/butylamine (amines), and thionaphthol/cysteine/N-acetylcysteine (thiols)—with triplicate analyses confirming reproducibility, while labeled product stability was monitored at 48-h intervals over 7 days under light-protected storage at 4 °C.

Data Processing and Statistical Analysis. The analytical workflow comprised data processing, quantification, and statistical analysis. First, raw LC-HRMS data were converted

https://doi.org/10.1021/acs.analchem.5c05834
Anal. Chem. 2025, 97, 26830−26841

(.mzXML via MSConvert) and processed through MZmine for feature extraction. The features were then aligned leveraging boron's isotopic signature (MATLAB) and matched (Python). Subsequently, relative quantification was achieved through normalization against an internal standard. Finally, statistical analysis included OPLS-DA (validated by permutation tests) with VIP calculation, hierarchical clustering with heatmaps, screening of significant metabolites by volcano plots, and pathway enrichment analysis via MetaboAnalyst (https://www.metaboanalyst.ca). Detailed procedures for data processing and relative code are described in the Supporting Information.

RESULTS AND DISCUSSION

Fabrication and Characterization of the Magnetic Chemoselective Probe. Figure 2a illustrates the synthetic route for the magnetic chemoselective polymeric probes. First, Fe_3O_4 nanoparticles were coated with silica via the Stöber method to produce silica-encapsulated magnetic cores Fe_3O_4@SiO_2, step (i). Surface vinylation was then achieved using γ-methacryloxypropyltrimethoxysilane (γ-MAPS), yielding vinyl-functionalized particles Fe_3O_4@SiO_2@γ-MAPS, step (ii). Next, a porous polymer shell was formed on the particle surface by distillation−precipitation polymerization of 3-methacrylamide-dopamine (3-MDA) and ethylene glycol dimethacrylate (EGDMA), introducing cis-diol functionalities Fe_3O_4@SiO_2@P(3-MDA-*co*-EGDMA), magnetic substrate, step (iii). Finally, chemoselective labeling reagents targeting carboxyl, amino, or thiol groups were introduced via a 30 min room-temperature incubation (step iv, Figure 2b). Taking the carboxyl probe as an example, we characterized the resulting material using scanning electron microscopy (SEM), energy-dispersive X-ray spectroscopy (EDS), X-ray photoelectron spectroscopy (XPS), and vibrating sample magnetometry (VSM). SEM images (Figure 2c) revealed a transformation from smooth, polydisperse Fe_3O_4 nanoparticles (100 nm) into uniform, rough-surfaced spheres (∼200 nm) after silica coating, confirming the formation of Fe_3O_4@SiO_2. Through the polymer coating process, magnetic substrate further developed a spherical morphology, with the average particle size increasing to 350 nm. The MCP(COOH) sample, serving as the final probe, exhibited a uniform spherical morphology and maintained a stable particle size of approximately 350 nm, demonstrating minimal further size increase. EDS analysis (Figure 2d) confirmed the presence of six elements (C, O, N, Fe, Si, and B) on the probe surface. EDS mapping of Si showed a clear silica shell with a thickness of ∼50 to 100 nm. XPS-Full scan results (Figure 2e) revealed that the intensities of the C 1s and N 1s peaks in the probe were higher than those in the magnetic substrate, indicating increased carbon and nitrogen content on the probe surface. For the key element boron, a characteristic B 1s peak emerged at 191.5 eV in the magnetic probe after introducing the boron-containing cis-dihydroxy structure (Figure 2f),[52−55] which was absent in the magnetic substrate. VSM analysis demonstrated superparamagnetic behavior at all synthetic stages (Figure 2g). Although the saturation magnetization decreased from 121.9 emu/g (bare Fe_3O_4) to 56.2 emu/g (final probe) due to successive coating steps, this value remains well above the practical threshold (∼16.3 emu/g) required for efficient magnetic separation, as previously reported by Ma et al.[56] Together, these results confirm the successful synthesis of magnetic chemoselective polymeric probes targeting carboxyl, amino, and thiol metabolites.

We systematically optimized the key parameters for the labeling reactions using these three probes, including probe dosage, the volume ratio of catalyst to sample, labeling time, and number of elution cycles (Figure S1−S4). Under the optimized conditions, efficient labeling of carboxyl, amino, and thiol metabolites was achieved within 30 min. This rapid reaction efficiency can be attributed to two major factors. First, the probes surfaces have abundant mesopores, which allow small-molecule metabolites to be readily enriched into the porous network and access the reactive sites, while larger biomolecules such as cell debris, proteins, and nucleic acids are excluded. Moreover, the confined environment within the mesopores may promote accelerated reaction kinetics due to the nanoscale confinement effect.[42] Second, the probes feature a high density of reactive sites. Quantitative analysis using standard calibration curves revealed that the carboxyl, amino, and thiol probes exhibit reactive site densities of 236.83 nmol/mg, 37.64 nmol/mg, and 33.85 nmol/mg, respectively—representing at least a 40-fold improvement over previously reported magnetic chemoselective probes[35] (Figure S5). Furthermore, the three probes successfully labeled a panel of 33 structurally diverse standards (12 carboxyl, 10 amino, and 11 thiol group metabolites, Table S1), demonstrating excellent probe universality and chemoselectivity (Figures S6−S8). These results validate the broad applicability of the probes for downstream submetabolome analysis.

Building of High-Throughput and High-Coverage Magnetic Chemoselective Labeling Strategy Based on Boron Beacon and Their Diagnostic MS^2 Fragment Ions. Parallel use of multiple chemoselective probes is the most straightforward approach to increase labeling coverage.[48] However, such strategies often suffer from high costs due to complex probe synthesis, expensive stable isotope reagents, and extended labeling times. Moreover, each probe-labeled sample typically requires separate LC-MS injections, significantly increasing analytical throughput time. In our workflow, we performed orthogonal labeling of carboxyl (A: -COOH), amino (B: -NH_2), and thiol (C: -SH) groups in a multiwall plate using the respective probes, followed by magnetic separation and elution. The three eluates were then pooled into a single sample for subsequent LC-HRMS analysis (Figure 1b). After processing the raw spectral data with MSconvert and MZmine software (including peak alignment, isotope filtering, etc.), the data were converted into a data matrix (Figure 3a). The boron isotopic pattern, with a natural abundance ratio of ^{10}B to ^{11}B of 0.248, served as a distinctive MS^1 beacon for rapid and accurate recognition of labeled metabolites.[42] Importantly, under higher-energy collisional dissociation (HCD) mode, each class of labeled metabolites exhibited characteristic MS^2 fragmentation patterns, allowing simultaneous identification of different functional groups (Figure 3a). Based on MS^2 spectra from 33 structurally diverse standards, we summarized three major fragmentation rules. (1) Each functional group produced unique diagnostic fragments from the labeling reagent: -SH: m/z 91.0542, 135.0632, 152.0877; -NH_2: m/z 105.0335, 122.0600, 149.0405, 166.0670; -COOH: m/z 105.0699, 122.0964, 131.0663, 149.0768, 166.1034. (2) A characteristic cleavage of the C−B bond yielded a $[M+H-44.0070]^+$ fragment. (3) Loss of one water molecule produced a $[M+H-18.0106]^+$ fragment. As representative examples, the MS^2 spectra of valeric acid (Figure 3b), butylamine (Figure 3c), and

https://doi.org/10.1021/acs.analchem.5c05834
Anal. Chem. 2025, 97, 26830−26841

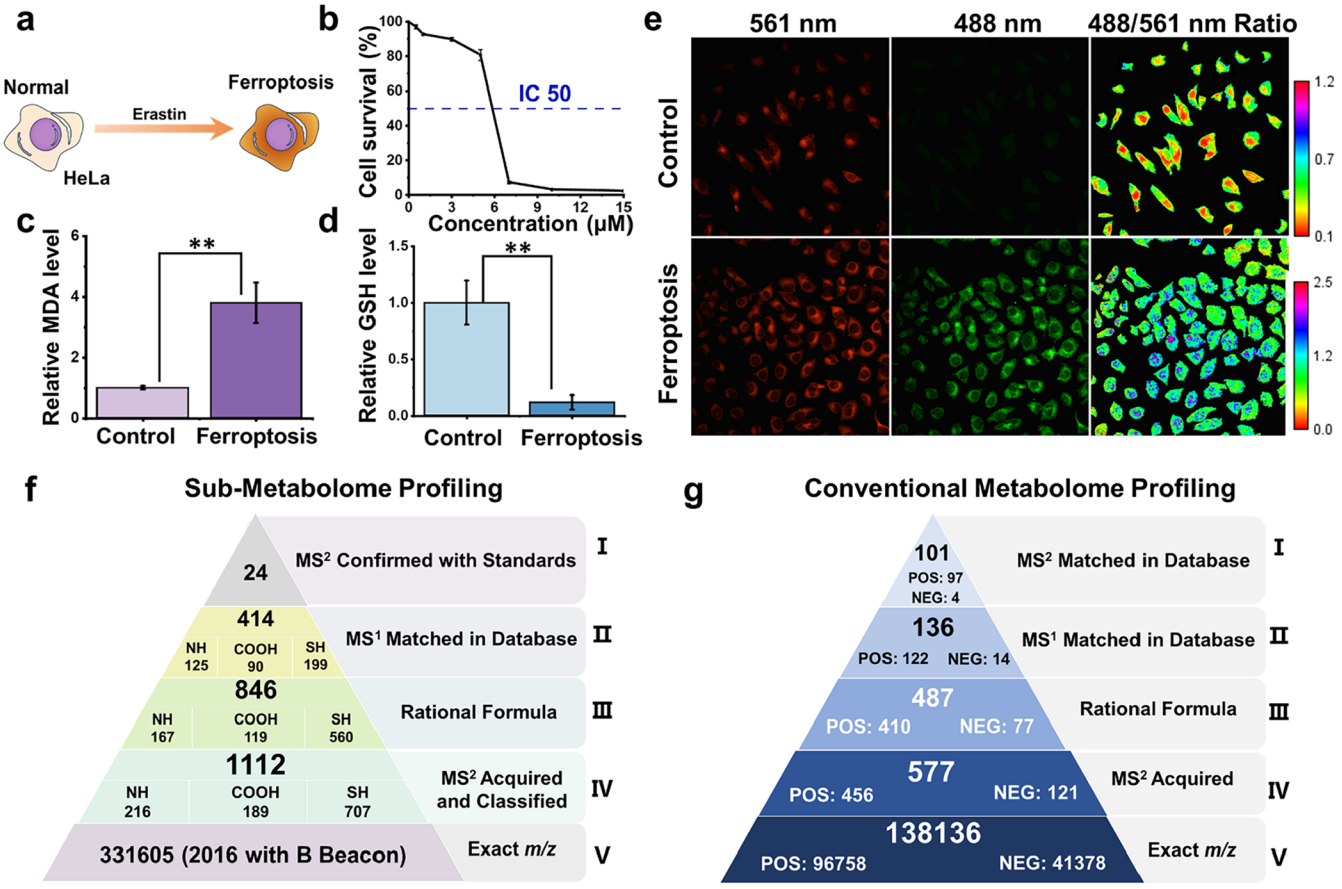

Figure 4. Submetabolome profiling of ferroptosis progression in HeLa cells induced by Erastin. (a) Schematic of ferroptosis induction in HeLa cells. (b) Erastin-induced Cytotoxicity: Cell viability of HeLa cells treated with 0−15 μmol/mL Erastin for 12 h was measured using the CCK-8 assay. (c) MDA Quantification: Malondialdehyde (MDA) levels, reflecting lipid peroxidation during ferroptosis, were quantified via thiobarbituric acid (TBA) assay at 532 nm. Elevated MDA content indicates oxidative damage to cell membranes. (d) GSH Content Assessment: Reduced glutathione (GSH) levels were evaluated by 5,5′-dithiobis(2-nitrobenzoic acid) (DTNB) assay at 412 nm. Depleted GSH signifies diminished cellular antioxidant capacity. (e) Lipid Peroxidation Detection: Erastin-treated HeLa cells were stained with BODIPY-C11 and imaged by confocal microscopy (excitation: 488/561 nm). Fluorescence intensity directly correlates with lipid peroxidation extent. (f) Functional group-specific submetabolome analysis based on chemoselective labeling. (g) Conventional untargeted metabolomics analysis of the same samples.

N-acetylcysteine (Figure 3d) were presented, highlighting the diagnostic ions for each labeled product. By leveraging the rule-based fragmentation pattern (particularly Rule 1), we were able to rapidly assign carboxyl-, amino-, and thiol-containing metabolites in a single MS analysis run time. Based on these rules, the presence of at least one diagnostic ion was sufficient for metabolite classification. A custom Python script enabled automated screening of diagnostic ions for functional group classification (Figure 3a). As shown in Figure S9−S11 and Tables S2−S4, all 33 spiked standards (12 carboxyl, 10 amino, and 11 thiol compounds) were successfully identified and correctly classified.

To evaluate the method's performance for qualitative and quantitative analysis in complex biological matrices, we conducted a methodological assessment using three parallel HeLa cell extract samples spiked with representative standards and internal controls. The selectivity of our probes was systematically ensured through multiple strategies: (1) Inherent selectivity of well-validated reactions (maleimide-thiol, NHS ester-amine, and amine-carboxyl amidation) at physiological pH; (2) Rigorous washing to remove physically adsorbed molecules; (3) Dual filtering criteria requiring both boron isotopic signature and class-specific MS^2 fragments for metabolite annotation; and (4) Successful labeling of all spiked standards, demonstrating probe specificity. The labeling efficiency for standards remained consistently above 70% (Tables S5−S7). Following LC-HRMS analysis, the relative standard deviation (RSD) of boron-tagged metabolite peak intensities was calculated across replicates. As shown in Figure S12a, 71% of detected features exhibited RSDs below 25%, indicating good reproducibility and method robustness. A one-week stability study further demonstrated that the labeled products remained stable throughout the test period (Figure S12b). The limits of detection (LODs) for labeled compounds ranged from 0.01 to 10.27 ng/mL, and limits of quantification (LOQs) ranged from 0.03 to 30.81 ng/mL. In contrast, the LODs for unlabeled standards spanned from 0.07 ng/mL to 326.09 μg/mL, highlighting the significantly improved sensitivity of the probe-based labeling strategy (Table S8). These integrated measures effectively minimized potential off-target binding and ensured high method specificity and data reliability.

Annotation of Thiol-, Amine-, and Carboxyl-Containing Metabolites During Early Ferroptosis. We established a ferroptosis model using the ferroptosis inducer Erastin and HeLa cells (Figure 4a). Initial optimization determined the optimal Erastin concentration. As shown in Figure 4b, coincubation with 7 μmol/mL Erastin for 12 h reduced cell

https://doi.org/10.1021/acs.analchem.5c05834
Anal. Chem. 2025, 97, 26830−26841

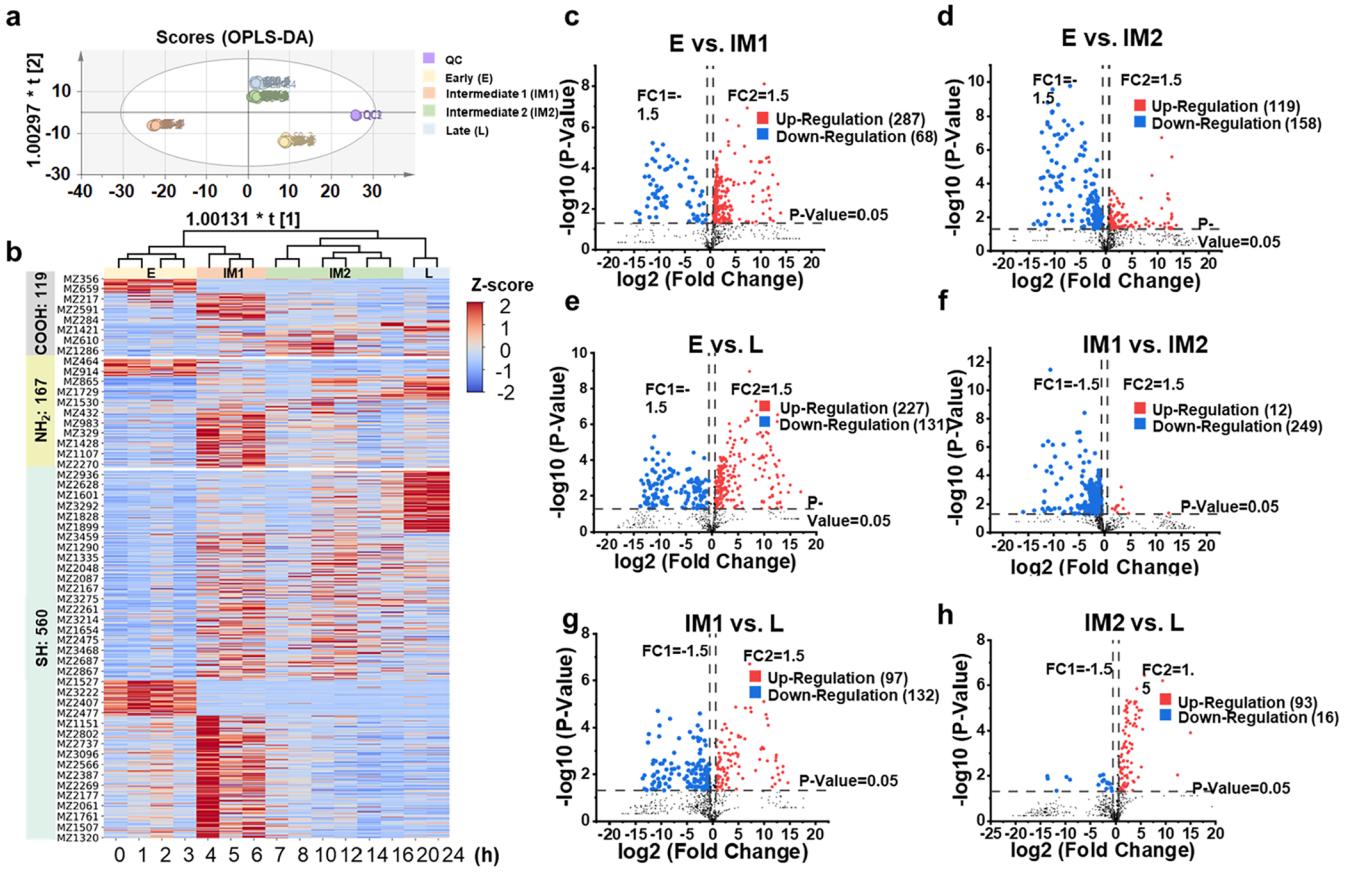

Figure 5. Statistical analysis of metabolites during cell homeostasis to ferroptosis. (a) OPLS-DA (orthogonal partial least-squares discriminant analysis) of 846 candidate metabolites across 24 h of induction. Four distinct metabolic stages of ferroptosis are resolved: early (E: 0, 1, 2, 3 h), intermediate 1 (IM1: 4, 5, 6 h), intermediate 2 (IM2: 7, 8, 10, 12, 14, 16 h), and late (L: 20, 24 h). (b) Heatmap showing temporal abundance patterns of the 846 candidate metabolites. Each column represents a time point (five biological replicates), and each row a metabolite. Relative intensities are Z-score normalized (blue to red indicates low to high abundance). Hierarchical clustering using Ward's method yields four sample clusters, consistent with OPLS-DA results. Volcano plot analysis of differential metabolites across four phases ($p < 0.05$, |fold change| ≥ 1.5). (c) Early vs Intermediate 1:287 metabolites were upregulated. 68 metabolites were downregulated. (d) Early vs Intermediate 2:119 metabolites were upregulated and 158 metabolites were downregulated. (e) Early vs Late: 227 metabolites were upregulated and 131 metabolites were downregulated. (f) Intermediate 1 vs Intermediate 2:12 metabolites were upregulated and 249 metabolites were downregulated. (g) Intermediate 1 vs Late: 97 metabolites were upregulated and 132 metabolites were downregulated. (h) Intermediate 2 vs Late: 93 metabolites were upregulated and 16 metabolites were downregulated.

viability to approximately 50%, establishing this concentration for subsequent experiments. The ferroptosis model was validated by assessing malondialdehyde (MDA) levels, glutathione (GSH) content, and lipid peroxidation. Thiobarbituric acid (TBA) assay revealed a 4-fold increase in MDA content in ferroptotic cells compared to controls, indicating significantly enhanced lipid peroxidation (Figures 4c and S13). Glutathione depletion, a hallmark of ferroptosis, was confirmed by 5,5′-dithiobis(2-nitrobenzoic acid) (DTNB) colorimetric analysis, showing an approximately 80% reduction in GSH levels in the ferroptosis group (Figure 4d). BODIPY-C11 fluorescence probing, the gold standard for detecting intracellular lipid peroxides, demonstrated markedly intensified oxidized (green) fluorescence signals in treated cells. The increased green/red fluorescence ratio further confirmed substantial accumulation of lipid peroxides, aligning with the characteristic biochemical features of ferroptosis (Figure 4e). Collectively, these results confirm the successful establishment of the Erastin-induced HeLa cell ferroptosis model.

We performed qualitative profiling of carboxyl-, amino-, and thiol-group-containing metabolites in ferroptotic cells using our magnetic chemoselective labeling strategy. As shown in Figure 4f, carboxyl-, amino-, and thiol-containing metabolites were labeled and analyzed via LC-HRMS. After raw data processing with MZmine 3.9.0, a total of 331,605 MS features were detected, among which 2,016 carried the boron isotopic signature, highlighting the high background noise in untargeted metabolomics. Subsequent MS^2 analysis of these B-tagged features yielded 1112 MS^2 spectra. Classification and molecular formula prediction using our Python-based algorithm identified 846 putative metabolites: 560 thiol-, 167 amino-, and 119 carboxyl-containing species. Cross-referencing with public databases (HMDB and METLIN) matched 414 putative metabolites (Table S9−S11), and 24 were further confirmed using in-house standards (Figures S14−S37). For comparison, the same samples were analyzed using a conventional untargeted LC-HRMS workflow (Figure 4g). Although a comparable number of MS^1 features were detected, only 577 features yielded high-quality MS^2 spectra—roughly half of those acquired using the probe-based method. After formula prediction, 487 plausible molecular formulas were obtained, of which only 136 (~28%) matched database entries

https://doi.org/10.1021/acs.analchem.5c05834
Anal. Chem. 2025, 97, 26830−26841

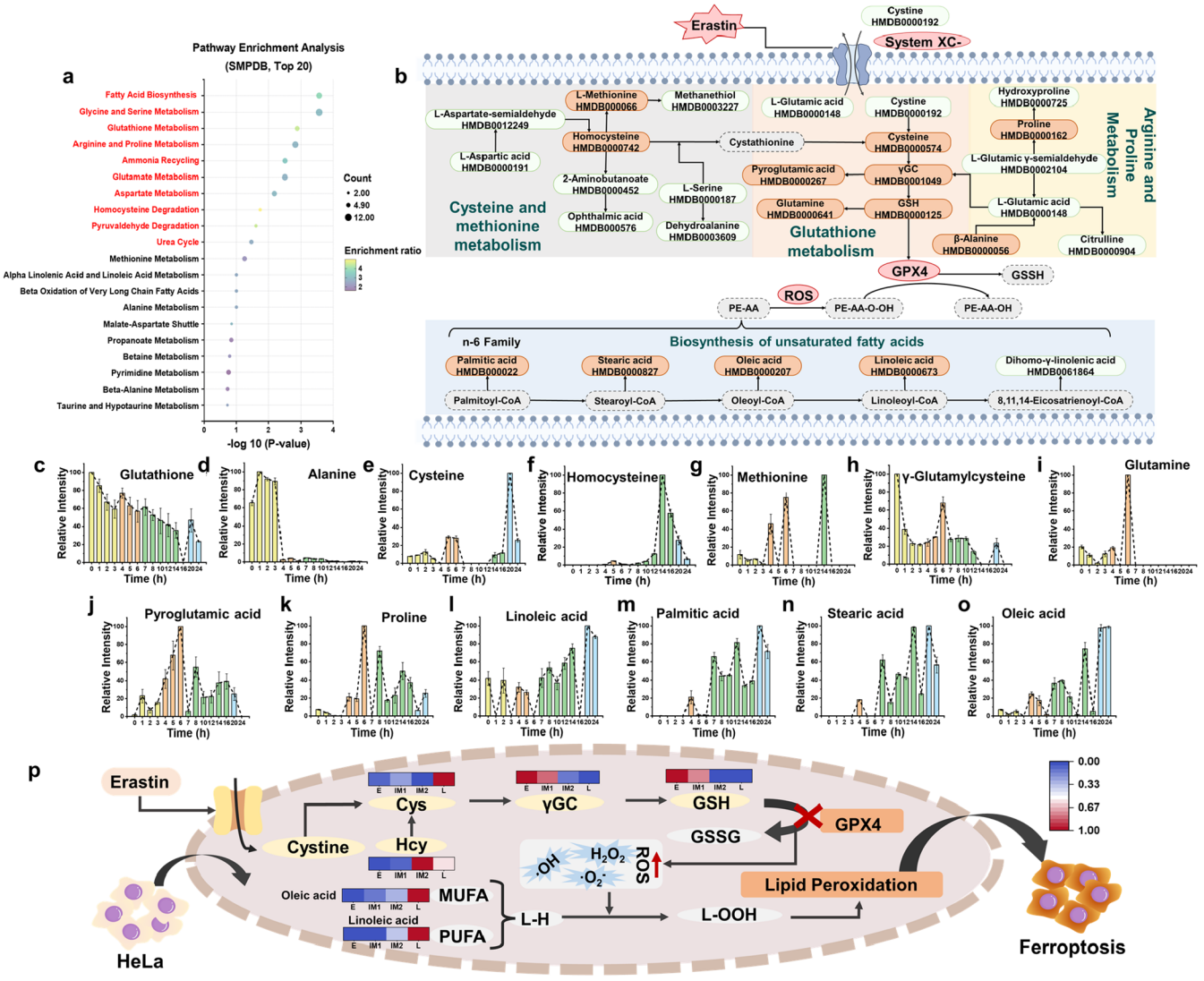

Figure 6. Enrichment pathway analysis and relative quantification of differential metabolites. (a) The top 20 metabolic pathways in ferroptotic cells after pathway enrichment analysis, based on the SMPDB database. Ten pathways were significantly enriched ($p < 0.05$) and are closely related to ferroptosis, including fatty acid biosynthesis, glycine-serine metabolism, glutathione metabolism, arginine-proline metabolism, the urea cycle, glutamine metabolism, aspartate metabolism, homocysteine degradation, pyruvaldehyde degradation, and ammonia recycling. (b) Putative involvement of thiol-, amine-, and carboxyl-containing metabolites in ferroptosis-related pathways. (c–o) Relative quantification of selected metabolites identified via our probe-labeling strategy. (p) Dynamic changes of representative metabolites in key pathways during early ferroptosis.

based on MS^1 information alone. In contrast, the submetabolome profiling had 414 (~49%) matched database entries based on MS^1 information. Notably, although our current workflow was performed solely in positive ionization mode, it identified approximately three times more putative metabolites than the conventional method, which utilized both positive and negative mode switching. Furthermore, 385 of the 414 metabolites identified by our labeling method were uniquely detected. As detailed in Table S12, our method achieved exceptional enrichment across all three functional groups, with unique detection rates exceeding 90% for each class, demonstrating that its value extends far beyond thiol metabolites alone. A direct comparison with the conventional method (Table S13) reveals that while conventional detection captured 54.4% of carboxyl and 84.0% of amino metabolites relative to our method, it completely failed to detect any thiol metabolites (0%). This indicates that even for amino and carboxyl metabolites with supposedly good MS responses, our method significantly outperforms in the number of metabolites detected, likely because the removal of matrix interference enables effective capture of numerous low-abundance amino and carboxyl metabolites that are otherwise missed by conventional analysis. Most strikingly, for poorly ionizing thiol metabolites, our method demonstrates an overwhelming advantage—without our labeling strategy, the entire thiol submetabolome remains essentially "invisible" in conventional analysis. This enhanced coverage is powerfully illustrated by the case of cysteine: as shown in Figure S38, this biologically critical metabolite was undetected in the conventional untargeted workflow, but our probe-based labeling dramatically enhanced its signal, enabling confident identification via MS^2 spectral matching with a synthetic standard. This example confirms the unique advantage of our method in detecting low-abundance metabolites that are otherwise obscured by matrix interference. In summary, our probe-based labeling method, through its matrix cleanup capability and signal enhancement

https://doi.org/10.1021/acs.analchem.5c05834
Anal. Chem. 2025, 97, 26830−26841

effect, is not only essential for hard-to-detect thiol metabolites but also crucial for substantially expanding the detection depth of amino and carboxyl metabolites. Frankly speaking, the conventional workflow ultimately identified more metabolites at the MS^2 level (101 compounds), whereas our submetabolome strategy achieved confident identification of only 24 metabolites by synthetic standards of the labeled products. This discrepancy primarily arises from the current lack of dedicated submetabolome databases and the limited availability of authentic standards. We believe that as this methodology gains broader adoption, more comprehensive databases and reference standards will become available, thereby further enhancing the qualitative power of submetabolome analysis.

Statistical Analysis of Metabolites During Cell Homeostasis to Ferroptosis. To monitor metabolic changes during ferroptosis, we treated HeLa cells with 7 μmol/mL Erastin and collected samples at 15 consecutive time points (three biological replicates per point). We systematically evaluated lipid peroxidation during Erastin-induced ferroptosis in HeLa cells across multiple time points. After staining with BODIPY-C11, fluorescence confocal microscopy (excitation: 488/561 nm) was used to monitor cell oxidative stress levels (Figure S39). Although the fluorescence signal distinguished cells with lipid peroxidation from those without, it lacked the resolution to differentiate oxidative stress levels across time points or to identify specific metabolites involved in the process. In contrast, our functional-group-specific metabolomics approach provided extensive metabolite-level information. Using SIMCA 14.1 software, we performed orthogonal partial least-squares discriminant analysis (OPLS-DA) on the 846 candidate metabolites (Figures 5a and S40a). Quality control (QC) samples clustered tightly, indicating good analytical stability and reproducibility. The ferroptosis progression over 24 h was clearly stratified into four phases: early (0, 1, 2, 3 h), intermediate-1 (4, 5, 6 h), intermediate-2 (7, 8, 10, 12, 14, 16 h), and late (20, 24 h). Among all detected features, 359 metabolites exhibited variable importance in projection (VIP) scores >1 (Figure S40b and Table S14). The model showed excellent performance, with cumulative R^2X(cum) = 0.805, R^2Y(cum) = 0.997, and Q^2(cum) = 0.860, all close to 1, indicating strong explanatory and predictive power. Permutation testing (n = 200) yielded R^2 = 0.931 and Q^2 = −0.604, suggesting good model fit and predictive ability without overfitting. A heatmap (Figure 5b) visualized the temporal abundance profiles of the 846 candidate metabolites. Hierarchical clustering based on Ward's method resolved the samples into four groups, consistent with the OPLS-DA classification. Further volcano plot analysis of the four stages (Figure 5c−h) identified 625 differential metabolites (p < 0.05, |fold change| ≥ 1.5), including 303 confidently matched putative compounds in HMDB database (highlighted in bold red in Tables S9−S11).

Enrichment Pathway Analysis and Relative Quantification of Differential Metabolites. We performed metabolite set enrichment analysis using MetaboAnalyst, mapping 303 differential metabolites with HMDB identifiers to the Small Molecule Pathway Database (SMPDB) (Figure 6a). Ten metabolic pathways (p < 0.05) were significantly enriched, including fatty acid biosynthesis, glycine-serine metabolism, glutathione metabolism, and others involving diverse carboxyl-, thiol-, and amine-containing metabolites (Table S15). Based on the qualitative results and pathway information from SMPDB and KEGG, we constructed a putative network of thiol-, amine-, and carboxyl-containing metabolites involved in ferroptosis (Figure 6b), and further conducted relative quantification of the identified primary metabolites (Figure S41). Erastin induces ferroptosis primarily by inhibiting System Xc^-, thereby blocking cystine uptake and leading to intracellular cysteine depletion. Consequently, glutathione (GSH) synthesis is impaired (Figure 6c).[57] Alanine, which can provide glutamate as a precursor for GSH biosynthesis,[58,59] showed a sharp decline after the early stage, potentially contributing to GSH reduction (Figure 6d). Notably, cysteine exhibited two distinct fluctuations during the ferroptosis process (Figure 6e), suggesting that its availability is not solely dependent on exogenous uptake. In mammalian cells, the transsulfuration pathway provides an alternative source of cysteine,[60] wherein homocysteine and serine are converted into cystathionine by cystathionine β-synthase (CBS), and subsequently into cysteine.[61] We observed that the transient elevation of homocysteine (Figure 6f) preceded the rebound in cysteine levels, confirming the activation of this compensatory transsulfuration pathway during ferroptosis. This compensatory mechanism explains the late-stage recovery of cysteine even as extracellular cystine import remained blocked. The subsequent sharp decline in homocysteine in the late stage is consistent with its consumption to fuel cysteine synthesis. Homocysteine also participates in methionine biosynthesis, and its fluctuation often leads to instability in methionine levels (Figure 6g). For example, as homocysteine is increasingly converted into cysteine during the late stage, methionine biosynthesis is diminished, resulting in decreased methionine levels. Downstream metabolites of cysteine, including γ-glutamylcysteine (Figure 6h), glutamine (Figure 6i), and pyroglutamate (Figure 6j), showed similar trends, with a notable synchronized upregulation at 6 h post-Erastin treatment, whereas the level of proline (Figure 6k) exhibited an initial increase followed by a subsequent decrease. Polyunsaturated fatty acids (PUFAs) in the plasma membrane are particularly susceptible to ROS attack, resulting in the formation of lipid hydroperoxides and subsequent membrane damage.[62] Adequate supply of linoleic acid is essential to sustain high levels of pro-ferroptotic PUFA-phospholipids.[63−65] We observed a time-dependent increase in linoleic acid abundance during Erastin treatment, consistent with progressive ferroptosis (Figure 6l). Although saturated fatty acids (SFAs) are not direct substrates for lipid peroxidation due to the lack of double bonds, they serve as precursors for PUFA synthesis.[65−67] Accordingly, levels of palmitic acid (Figure 6m) and stearic acid (Figure 6n) also increased during ferroptosis. In contrast, upregulation of oleic acid (Figure 6o), which reduces cellular PUFA levels via ACSL3-dependent incorporation into neutral lipids, has been shown to antagonize ferroptosis.[68−70] It can be observed that the dynamic changes of these distinct types of metabolites during the ferroptosis process are interwoven, forming an intricate and mutually regulatory network (Figure 6p). Nonetheless, metabolomics alone offers only a preliminary view of these dynamic metabolic changes. A more comprehensive understanding of the regulatory mechanisms underlying ferroptosis will require systematic integration of multiomics data, including transcriptomics and proteomics.

https://doi.org/10.1021/acs.analchem.5c05834
Anal. Chem. 2025, 97, 26830−26841

CONCLUSION

Chemical structure-guided submetabolome approach significantly reduces the inherent blindness in traditional metabolomics studies. By enabling targeted analysis of specific functional groups based on prior biochemical knowledge, it enhances sensitivity, coverage, and accuracy for metabolome characterization while minimizing data redundancy. To achieve this goal, we developed the novel magnetic chemoselective probes that streamlined the submetabolome enrichment and labeling procedure into a rapid 30 min workflow. Combining MS^1-level boron tagguided precursor recognition with MS^2-level diagnostic fragments targeting thiol, amine, and carboxyl groups, automated submetabolome annotation was achieved in a single LC-MS injection. We successfully applied this method to profile metabolome during early stage ferroptosis of HeLa cells, capturing 303 dysregulated metabolites with clearly defined functional groups. This work provides a new analytical strategy for functional group-oriented submetabolome analysis with high throughput, low cost, and broad coverage, facilitating deep functional annotation of complex metabolic systems. Looking forward, integration of this approach with upstream multiomics platforms such as transcriptomics and proteomics holds great promise for elucidating the underlying biological mechanisms governing metabolic regulation.

ASSOCIATED CONTENT

Supporting Information

The Supporting Information is available free of charge at https://pubs.acs.org/doi/10.1021/acs.analchem.5c05834.

Materials and probe synthesis details; optimization of labeling conditions; additional SEM, XPS, and VSM characterization data; reproducibility and stability assessments; limits of detection and quantification for labeled vs unlabeled metabolites; OPLS-DA model validation; pathway enrichment analysis; temporal profiles of key metabolites (PDF)

AUTHOR INFORMATION

Corresponding Authors

Wei-Hai Chen − *College of Chemistry and Molecular Sciences, Wuhan University, Wuhan, Hubei 430072, P. R. China;* orcid.org/0000-0003-3100-2319; Email: chenwei-hai@whu.edu.cn

Zhenwei Wei − *College of Chemistry and Molecular Sciences, Wuhan University, Wuhan, Hubei 430072, P. R. China;* orcid.org/0000-0001-7016-7787; Email: weizw2021@whu.edu.cn

Xiangyu Wang − *College of Chemistry and Molecular Sciences, Wuhan University, Wuhan, Hubei 430072, P. R. China; School of Public Health, Wuhan University, Wuhan, Hubei 430072, P. R. China;* orcid.org/0009-0007-5471-8594; Email: xywang2018@whu.edu.cn

Authors

Haijie Wang − *College of Chemistry and Molecular Sciences, Wuhan University, Wuhan, Hubei 430072, P. R. China*

Qian An − *College of Chemistry and Molecular Sciences, Wuhan University, Wuhan, Hubei 430072, P. R. China*

Wenxin Wang − *College of Chemistry and Molecular Sciences, Wuhan University, Wuhan, Hubei 430072, P. R. China*

Hao Zhou − *College of Chemistry and Molecular Sciences, Wuhan University, Wuhan, Hubei 430072, P. R. China*

Youping Deng − *Zhongnan Hospital of Wuhan University, Wuhan, Hubei 430071, P. R. China*

Yu-Qi Feng − *School of Bioengineering and Health, Wuhan Textile University, Wuhan, Hubei 430200, P. R. China;* orcid.org/0000-0003-1107-5385

Complete contact information is available at: https://pubs.acs.org/10.1021/acs.analchem.5c05834

Notes

The authors declare no competing financial interest.

ACKNOWLEDGMENTS

Z.W. acknowledges the National Key R&D Program of China (No. 2023YFF0723100), the National Natural Science Foundation of China (No. 22374110), and the Fundamental Research Funds for the Central Universities. X.W. acknowledges support from the National Natural Science Foundation of China (No. 22504100), the China Postdoctoral Science Foundation (Grant No. 2024M762465) and the open subsidies for large-scale instru-ments and equipment at Wuhan University. W.H.C. acknowl-edges the National Natural Science Foundation of China (No. 52273301 and 52473145). The authors thank the Test Center and Core Facility of Wuhan University for assistance with mate-rial characterizations and sample analysis.

REFERENCES

(1) Jiang, X.; Stockwell, B. R.; Conrad, M. *Nat. Rev. Mol. Cell Biol.* **2021**, *22* (4), 266−282.

(2) Park, M. W.; Cha, H. W.; Kim, J.; Kim, J. H.; Yang, H.; Yoon, S.; et al. *Redox Biol.* **2021**, *41*, No. 101947.

(3) Wang, M.; Hao, H.; Bai, P.; Wu, J.; Zhang, Z.; Liu, T.; et al. *Adv. Funct. Mater.* **2024**, *34* (44), No. 2407468.

(4) Zhang, F.; Li, F.; Lu, G.-H.; Nie, W.; Zhang, L.; Lv, Y.; et al. *ACS Nano* **2019**, *13* (5), 5662−5673.

(5) Dixon, S. J.; Lemberg, K. M.; Lamprecht, M. R.; Skouta, R.; Zaitsev, E. M.; Gleason, C. E.; et al. *Cell* **2012**, *149* (5), 1060−1072.

(6) Zeng, F.; Nijiati, S.; Tang, L.; Ye, J.; Zhou, Z.; Chen, X. *Angew. Chem., Int. Ed.* **2023**, *62* (35), No. e202300379.

(7) Sies, H.; Berndt, C.; Jones, D. P. *Annu. Rev. Biochem.* **2017**, *86* (1), 715−748.

(8) Ursini, F.; Maiorino, M.; Forman, H. J. *Redox Biol.* **2016**, *8*, 205−215.

(9) Schieber, M.; Chandel, N. S. *Curr. Biol.* **2014**, *24* (10), R453−R462.

(10) Ingold, I.; Berndt, C.; Schmitt, S.; Doll, S.; Poschmann, G.; Buday, K.; et al. *Cell* **2018**, *172* (3), 409−422.

(11) Song, X.; Zhu, S.; Chen, P.; Hou, W.; Wen, Q.; Liu, J.; et al. *Curr. Biol.* **2018**, *28* (15), 2388−2399.

(12) Jia, M.; Qin, D.; Zhao, C.; Chai, L.; Yu, Z.; Wang, W.; et al. *Nat. Immunol.* **2020**, *21* (7), 727−735.

(13) Yang, W. S.; Kim, K. J.; Gaschler, M. M.; Patel, M.; Shchepinov, M. S.; Stockwell, B. R. *Proc. Natl. Acad. Sci. U.S.A.* **2016**, *113* (34), E4966−E4975.

(14) Liao, P.; Wang, W.; Wang, W.; Kryczek, I.; Li, X.; Bian, Y.; et al. *Cancer Cell* **2022**, *40* (4), 365−378.

(15) Lee, J.-Y.; Nam, M.; Son, H. Y.; Hyun, K.; Jang, S. Y.; Kim, J. W.; et al. *Proc. Natl. Acad. Sci. U.S.A.* **2020**, *117* (51), 32433−32442.

(16) Alves, F.; Lane, D.; Nguyen, T. P. M.; Bush, A. I.; Ayton, S. *Signal Transduction Targeted Ther.* **2025**, *10* (1), 2−29.

(17) Floros, K. V.; Chawla, A. T.; Johnson-Berro, M. O.; Khatri, R.; Stamatouli, A. M.; Boikos, S. A.; et al. *Cell Stress* **2022**, *6* (2), 21−29.

(18) Liu, D.; Liang, C.-H.; Huang, B.; Zhuang, X.; Cui, W.; Yang, L.; et al. *Adv. Sci.* **2023**, *10* (6), No. 2204006.

(19) Hirayama, T.; Tsuboi, H.; Niwa, M.; Miki, A.; Kadota, S.; Ikeshita, Y.; et al. *Chem. Sci.* **2017**, *8* (7), 4858−4866.

(20) Li, H.; Shi, W.; Li, X.; Hu, Y.; Fang, Y.; Ma, H. *J. Am. Chem. Soc.* **2019**, *141* (45), 18301−18307.
(21) Zhao, B.; Xu, X.; Wen, X.; Liu, Q.; Dong, C.; Yang, Q.; et al. *Anal. Chem.* **2024**, *96* (15), 5992−6000.
(22) Wang, Y.; Yan, H.; Yue, Y.; Zhang, Y.; Huo, F.; Cheng, F.; Yin, C. *Chem. Eng. J.* **2023**, *464*, No. 142496.
(23) Wang, K.-N.; Liu, L.-Y.; Mao, D.; Xu, S.; Tan, C.-P.; Cao, Q.; et al. *Angew. Chem., Int. Ed.* **2021**, *60* (27), 15095−15100.
(24) Wang, S.-Y.; Qu, Y.-C.; Shao, N.; Niu, L.-Y.; Yang, Q.-Z. *Anal. Chem.* **2024**, *96* (11), 4570−4579.
(25) Jiang, X.; Chen, J.; Bajić, A.; Zhang, C.; Song, X.; Carroll, S. L.; et al. *Nat. Commun.* **2017**, *8* (1), No. 16087.
(26) Reimers, N.; Do, Q.; Zhang, R.; Guo, A.; Ostrander, R.; Shoji, A.; et al. *J. Am. Soc. Mass. Spectrom.* **2023**, *34* (9), 2016−2024.
(27) Zeng, Y.; Yang, J.; Gu, Z.; Liu, H.; Cheng, Y.; Peng, R.; et al. *Anal. Chem.* **2025**, *97* (13), 7278−7288.
(28) Saimoto, Y.; Kusakabe, D.; Morimoto, K.; Matsuoka, Y.; Kozakura, E.; Kato, N.; et al. *Nat. Commun.* **2025**, *16* (1), No. 3554.
(29) Zheng, F.; Zhao, X.; Zeng, Z.; Wang, L.; Lv, W.; Wang, Q.; Xu, G. *Nat. Protoc.* **2020**, *15* (8), 2519−2537.
(30) Lv, W.; Wang, L.; Xuan, Q.; Zhao, X.; Liu, X.; Shi, X.; Xu, G. *Anal. Chem.* **2020**, *92* (8), 6043−6050.
(31) Li, H.; Qin, Q.; Qiao, L.; Shi, X.; Xu, G. *Chem. Commun.* **2015**, *51* (56), 11321−11324.
(32) Carlson, E. E.; Cravatt, B. F. *Nat. Methods* **2007**, *4* (5), 429−435.
(33) Hoki, J. S.; Le, H. H.; Mellott, K. E.; Zhang, Y. K.; Fox, B. W.; Rodrigues, P. R.; et al. *J. Am. Chem. Soc.* **2020**, *142* (43), 18449−18459.
(34) Garg, N.; Conway, L. P.; Ballet, C.; Correia, M. S. P.; Olsson, F. K. S.; Vujasinovic, M.; et al. *Angew. Chem., Int. Ed.* **2018**, *57* (42), 13805−13809.
(35) Lin, W.; Conway, L. P.; Vujasinovic, M.; Löhr, J.-M.; Globisch, D. *Angew. Chem.* **2021**, *133* (43), 23420−23428.
(36) Alexandrov, T. *Nat. Metab.* **2023**, *5* (9), 1443−1445.
(37) Alseekh, S.; Aharoni, A.; Brotman, Y.; Contrepois, K.; D'Auria, J.; Ewald, J.; et al. *Nat. Methods* **2021**, *18* (7), 747−756.
(38) Liu, S.; Yu, M.; Luo, X.-Y.; Liu, J.; Zou, Z.-M. *Adv. Sci.* **2025**, *12* (13), No. 2413830.
(39) Chen, J.; Tian, Y.; Zhang, Y.-X.; Xu, F.-G. *J. Anal. Test* **2020**, *4*, 175−182.
(40) Conway, L. P.; Garg, N.; Lin, W.; Vujasinovic, M.; Löhr, J.-M.; Globisch, D. *Chem. Commun.* **2019**, *55* (62), 9080−9083.
(41) Lin, W.; Conway, L. P.; Block, A.; Sommi, G.; Vujasinovic, M.; Löhr, J.-M.; Globisch, D. *Analyst* **2020**, *145* (11), 3822−3831.
(42) Wang, X.; Bai, P.; Li, Z.; Zhu, Q.-F.; Wei, Z.; Feng, Y.-Q. *Angew. Chem., Int. Ed.* **2022**, *61* (44), No. e202208138.
(43) Wang, W.; Yang, Y.; Chen, Z.; Wang, X.; Zhang, G.-L.; He, T.; et al. *Anal. Chem.* **2024**, *96* (2), 787−793.
(44) Fu, X.-K.; Han, S.-Q.; Ha, W.; Shi, Y.-P. *J. Agric. Food Chem.* **2023**, *71* (40), 14814−14824.
(45) Zhang, M.; Lai, Z.; Zhang, R.; Liu, S.; Tian, H.; Qiu, Y.; et al. *Small* **2023**, *19* (1), No. 2204734.
(46) Takeuchi, T.; Kubota, T.; Nakanishi, Y.; Tsugawa, H.; Suda, W.; Kwon, A. T.-J.; et al. *Nature* **2023**, *621* (7978), 389−395.
(47) Hicks, K. G.; Cluntun, A. A.; Schubert, H. L.; Hackett, S. R.; Berg, J. A.; Leonard, P. G.; et al. *Science* **2023**, *379* (6636), 996−1003.
(48) Tian, H.; Lai, Z.; Zhang, W.; Zhang, M.; Yang, X.; Zhou, J.; Li, Z. *Small Methods* **2024**, *8* (12), No. 2400529.
(49) Ye, L.; Dong, X.-M.; Miao, P.-R.; Xu, Y.-X.; Wu, P.; Zhao, J.-L.; et al. *Chem. Eng. J.* **2025**, *508*, No. 160878.
(50) Lin, W.; Gerullat, L.; Braadland, P. R.; Fournier, A.; Hov, J. R.; Globisch, D. *Angew. Chem., Int. Ed.* **2024**, *63* (14), No. e202318579.
(51) Liu, Z.; Cai, B.-D.; Feng, Y.-Q. *J. Chromatogr. B* **2012**, *891*−*892*, 27−35.
(52) Gao, W.; Wang, Z.; Zhang, Y.; Shen, C.; Wang, Y.; Zhan, L. *Appl. Surf. Sci.* **2024**, *669*, No. 160459.
(53) Zhou, B.; Deng, T.; Yang, C.; Wang, M.; Yan, H.; Yang, Z.; et al. *Adv. Funct. Mater.* **2023**, *33* (13), No. 2212005.
(54) Li, Z.; Li, X.; Zhang, Y.; Ren, T.; Zhao, Y.; Zeng, X.; van der Heide, E. *Appl. Surf. Sci.* **2014**, *308*, 91−99.
(55) Yun, J.; Chen, L.; Zhang, X.; Feng, J.; Liu, L. *Polymers* **2016**, *8* (3), 35.
(56) Ma, Z.; Guan, Y.; Liu, H. *J. Polym. Sci., Polym. Chem.* **2005**, *43* (15), 3433−3439.
(57) Yang, W. S.; SriRamaratnam, R.; Welsch, M. E.; Shimada, K.; Skouta, R.; Viswanathan, V. S.; et al. *Cell* **2014**, *156* (1), 317−331.
(58) Sookoian, S.; Pirola, C. J. *World J. Gastroenterol.* **2012**, *18* (29), 3775.
(59) Ellinger, J. J.; Lewis, I. A.; Markley, J. L. *J. Biomol. NMR* **2011**, *49*, 221−229.
(60) Liu, N.; Lin, X.; Huang, C. *Br. J. Cancer* **2020**, *122* (2), 279−292.
(61) Xi, C.; Pang, J.; Xue, W.; Cui, Y.; Jiang, N.; Zhi, W.; et al. *Commun. Biol.* **2025**, *8* (1), 15.
(62) Liang, D.; Minikes, A. M.; Jiang, X. *Mol. Cell* **2022**, *82* (12), 2215−2227.
(63) Lee, J.-Y.; Kim, W. K.; Bae, K.-H.; Lee, S. C.; Lee, E.-W. *Biology* **2021**, *10* (3), 184.
(64) Kim, J. W.; Lee, J.-Y.; Oh, M.; Lee, E.-W. *Exp. Mol. Med.* **2023**, *55* (8), 1620−1631.
(65) Sokol, K. H.; Lee, C. J.; Rogers, T. J.; Waldhart, A.; Ellis, A. E.; Madireddy, S.; et al. *Cell Chem. Biol.* **2025**, *32* (3), 408−422.
(66) Stockwell, B. R. *Cell* **2022**, *185* (14), 2401−2421.
(67) Mashima, T.; Seimiya, H.; Tsuruo, T. *Br. J. Cancer* **2009**, *100* (9), 1369−1372.
(68) Ubellacker, J. M.; Tasdogan, A.; Ramesh, V.; Shen, B.; Mitchell, E. C.; Martin-Sandoval, M. S.; et al. *Nature* **2020**, *585* (7823), 113−118.
(69) Mann, J.; Reznik, E.; Santer, M.; Fongheiser, M. A.; Smith, N.; Hirschhorn, T.; et al. *Cell Chem. Biol.* **2024**, *31* (2), 249−264.
(70) Cao, Y.; Li, J.; Chen, Y.; Wang, Y.; Liu, Z.; Huang, L.; et al. *Cell Death Dis.* **2025**, *16* (1), 1−13.

https://doi.org/10.1021/acs.analchem.5c05834
Anal. Chem. 2025, 97, 26830−26841